Research Article

Blast Liquefaction Test of Saturated Sand Foundations Disposed by a Drainage Rigid Pile

Songtao Ni,[1] Yumin Chen [ID],[1] Runze Chen,[1] Hanlong Liu,[2] Changchun Li,[1] and Shaobin Hu [ID][1]

[1]*College of Civil and Transportation Engineering, Hohai University, Nanjing 210098, China*
[2]*College of Civil Engineering, Chongqing University, Chongqing 400450, China*

Correspondence should be addressed to Yumin Chen; ymch@hhu.edu.cn

Drainage rigid piles represent a commonly used antiliquefaction treatment for saturated sand foundations. Small-scale model tests on the liquefaction-resistant characteristics of drainage rigid piles subjected to blasting were conducted in this study. The effect of ordinary rigid piles and drainage rigid piles on the disposal of saturated sand foundations was investigated by using carbon dioxide (CO_2) fracturing to generate explosive vibratory loads. The test results showed that the blast vibration load increased the relative density of the site by approximately 10% and that the relative density was proportional to the burial depth. The site vertical acceleration attenuations resulting from the two blasts were 35% and 45%, respectively, and the variation pattern of vertical acceleration on both sides of drainage rigid piles and ordinary piles is similar. Drainage rigid piles can dissipate more than 70% of the excess pore water pressure under liquefaction and can quickly accumulate excess pore water pressure and, likewise, quickly dissipate excess pore water pressure. The higher the excess pore water pressure at a site is, the more effective the disposal by a drainage rigid pile is. This field test provides a design reference for the engineering application of drainage rigid piles.

1. Introduction

According to the statistics obtained in previous surveys, most earthquake damage to geotechnical structures is caused by the liquefaction of foundation soils [1–3]. Sand liquefaction is under the action of cyclic loading when caused by earthquakes; if the saturated sand cannot be drained, the stress borne by the soil skeleton will be transferred to the pore water, resulting in a reduction of the effective stress, thus causing the loss of strength and stiffness of the soil and causing deformation of the soil layer [4–7]. Depending on the mechanism of seismic liquefaction, antiliquefaction measures for saturated sand foundations can be divided into two major categories: one method is to improve the soil quality, and the other is to change the soil stress. The common methods for improving soil quality include the replacement method [8], compacting method [9], and enclosure method [10]. The methods used to change the soil stress include pressurization [11], drainage [12], and pile foundations [13]. Currently, the most common application in engineering is still flexible pile methods with drainage properties, such as extruded sand piles and gravel piles, which account for more than half of the actual applications [14]. However, these flexible piles have a limited treatment depth, and for high-rise buildings, rigid piles are commonly used to achieve a certain bearing capacity. Because rigid piles themselves do not have drainage channels, when an earthquake occurs the saturated sand foundation produces liquefaction, and the excess pore water pressure accumulated in the soil around the pile cannot be quickly dissipated, thereby resulting in a series of seismic damages.

Since the main reason for the damage of rigid piles in liquefied foundations is that the excess pore water pressure generated by the soil around the piles cannot be effectively dissipated, some scholars have begun attempting to add drainage channels to rigid pile foundations to improve the

seismic performance of rigid piles in liquefied foundations. Yasuda et al. studied the effect of using sheet piles with drainage channels in reducing embankment settlement and suggested that sheet piles with drainage channels are more effective than ordinary sheet piles [15]. Otsushi et al. investigated the effectiveness of drainage sheet pile treatment of aqueducts and flume structures against liquefaction [16]. Subsequent research further showed that this method can stop the lateral flow of the soil inside the enclosure when an earthquake triggers the liquefaction of the site soil to reduce the settlement of the superstructure due to liquefaction and the uplift displacement of the underground structure [17, 18].

However, most of the research on drainage rigid pile treatment of saturated sand foundations is limited to indoor shaking table tests, and the test scale is far from the actual engineering field requirements. Therefore, in this study, blast vibration is used to achieve near-prototype liquefaction site conditions for saturated sand foundations [19–22] to investigate the characteristics of drainage rigid piles for the disposal of blast liquefaction of saturated sand foundations. High-energy gas fracturing technology has been developed internationally [23–28]. In this paper, the blast vibration effect required for the test was obtained by using carbon dioxide pneumatic fracturing [29], and the acceleration response of the site was monitored. According to the vibration conditions generated by CO_2 pneumatic fracturing at different air pressures, the changes in acceleration and pore water pressure around ordinary piles and drainage rigid piles were compared and analyzed, and the relative density of the site before and after the test was tested to evaluate the disposal of saturated sand foundations via drainage rigid piles.

2. Materials and Methods

2.1. In-Site Conditions. Based on the necessary blast vibration conditions, an open site in Fenghuang Mountain, Jiangning District, Nanjing, was chosen for the field test. The equipment layout and site photos are shown in Figure 1. The circular test pit dug at the site was 2.8 m in diameter and 1.2 m deep, with clay soil at the bottom and around the pit. Two groups of carbon dioxide-fracturing containers were buried at the bottom of the pit at a depth of 0.5 m. Vessels 1–4 in Figure 1 were used for the first test, where the mass of dry ice in each container was 450 g. Vessels 5–8 were used for the second test, where the mass of dry ice in each container was 680 g. Each set of vessels was arranged symmetrically for the two piles to be laid out to allow a comparison of the difference in the peripheral acceleration and pore pressure between the two under the same blast vibration. After the fracturing vessel was buried, the bottom of the pit was paved with 0.2 m of Yangtze River gray sand to protect the waterproof membrane from being laid on top and prevent the impact of blasts from damaging the membrane. Two acceleration sensors were placed at the bottom of the pit to monitor the vertical acceleration generated by the blast vibration at the bottom of the pit to be used to compare with the results of subsequent numerical simulations.

After laying the waterproof membrane, the ordinary pile and drainage rigid pile will be symmetrically arranged, as shown in Figure 1. The spacing between the two is 0.8 m, where the drainage rigid pile on the drainage body side faces the pit wall arrangement. After the two piles were laid out, water storage began, and the Yangtze River gray river sand was filled in layers using the pluviation method to a total depth of 0.8 m. Three pore water pressure sensors and three acceleration sensors were placed along the depth of the drainage body side of the drainage rigid piles, as shown in Figure 1, with the acceleration sensors placed 10 cm outside of the pore water pressure sensors.

The sand used in the test is Yangtze River gray sand, whose dry density is 1 523 kg/m³ and whose saturation density is 1,943 kg/m³. The specific gravity of the soil particles is 2.622, which is expressed by G_s. Other basic physical and mechanical parameters are shown in Table 1, where C_u is the inhomogeneity coefficient and e is the pore ratio. The gradation curves are shown in Figure 2.

The sand in the backfill of the test excavation pit is poorly graded, uniform fine sand, and according to the particle size and combined with previous blast liquefaction tests, the sand is highly susceptible to liquefaction under a blast load [30].

2.2. Test Equipment. The blast equipment used in the test is a CO_2 pneumatic fracturing vessel [29], which works on the principle of rapid combustion of a CO_2 fusion agent in CO_2, releasing a large amount of heat to promote the rapid vaporization of dry ice powder, thus forming a transient high pressure in a closed space and finally achieving the fracturing effect. By adjusting the activity and heat value of the CO_2 fusion agent, the pressure rise rate and action time can be effectively controlled, which can avoid a transient strong shock disturbance and noise, but can also achieve a more ideal dynamic loading rate. The fracturing vessel and the fracturing principle are shown in Figure 3. The ratio of the mass of dry ice to the mass of the carbon dioxide fusion agent is called mass ratio. By adjusting different mass ratios, different fracturing effects can be obtained, generally speaking, the best effect is achieved when the mass ratio reaches 8.

Using the above carbon dioxide-fracturing vessel, according to different mass ratios of dry ice powder and carbon dioxide fusion agent, different fracturing effects can be obtained in order to achieve the effect of different blast vibrations in this experiment. In this test, the fracturing vessel for the first test was a low mass ratio vessel, as shown in Figure 1(a) with numbers 1–4, and the fracturing sequence was four vessels fractured at the same time. The fracturing vessels in the second test were high mass ratio vessels, as shown in Figure 1(a), numbers 5–8, and the fracturing sequence was 5 and 7 fractured simultaneously, followed by 8 and finally 6. Therefore, this experiment can be divided into simultaneous fracturing blast vibration tests and multiple fracturing blast vibration tests.

The drainage rigid pile used in the test was proposed by Prof. Han-long Liu et al. [31], and its dimensions and physical drawings are shown in Figure 4. In this test, the
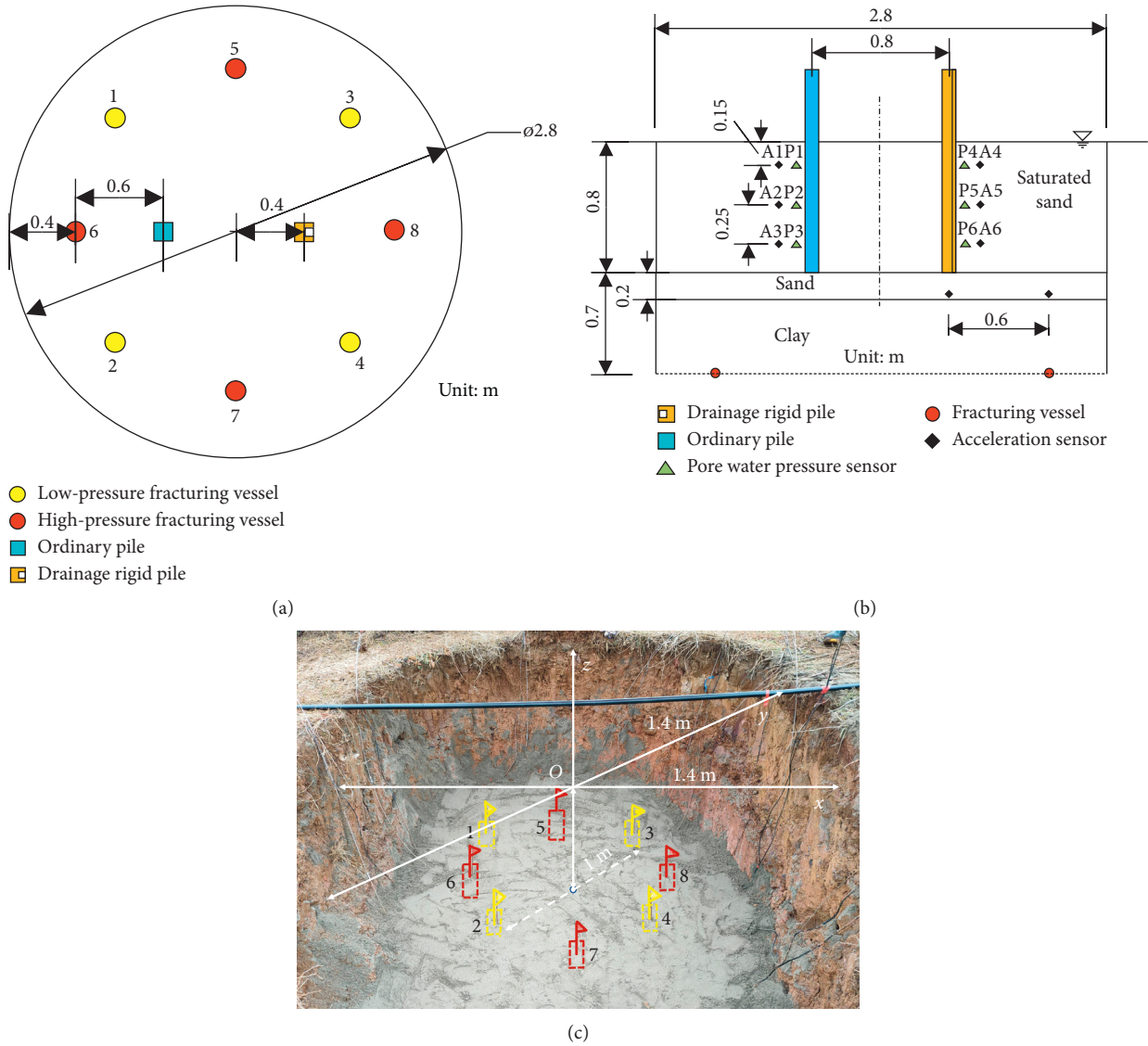
(a)

(b)

(c)

FIGURE 1: Site set-up scheme. (a) Number and location of the fracturing vessel, (b) site dimensions and equipment layout, and (c) schematic diagram of the actual vessel location onsite.

TABLE 1: Basic physical properties of the Yangtze River gray sand.

d_{60}/mm	d_{50}/mm	d_{10}/mm	C_u	G_s	e
0.28	0.24	0.16	1.76	2.622	0.72

similarity ratio considered was 1/10, the pile is buried at a depth of 0.8 m. The top section of the pile is a square with a side length of 4 cm. A prefabricated recess is provided on one side of the pile for placing the plastic drainage panel, and the drainage body is 2 cm wide and arranged along the pile body. The drainage panel is wrapped around by geotextile to prevent sand from entering it and blocking the drainage channel. The dimensions of the ordinary pile were the same as those of the drainage rigid pile.

Plastic drainage panels can form drainage channels through which excess pore water caused by blast vibration loads can flow out of the ground and reduce the excess pore water pressure in the foundation. The advantage of this type

of drainage rigid pile in engineering practice is that it has both the load-bearing performance of rigid piles and the drainage performance of gravel piles, which can mitigate and weaken the liquefaction natural disaster generated by saturated sand foundations. A schematic diagram of its principle is shown in Figure 5.

The finished site after the layout is shown in Figure 6.

2.3. Test Arrangement. Fracturing containers 1–4 in Figure 1 were filled with 450 g of dry ice, and the ambient temperature at the site was 2 degrees Celsius. The sand layer at the site before the blast vibration was probed with static cone penetration equipment to obtain the lateral friction resistance and the cone tip resistance at the corresponding depth.

After the completion of the blast vibration test, the sand layer was tested again via a static cone penetration test (CPT). The relative density before and after the blast
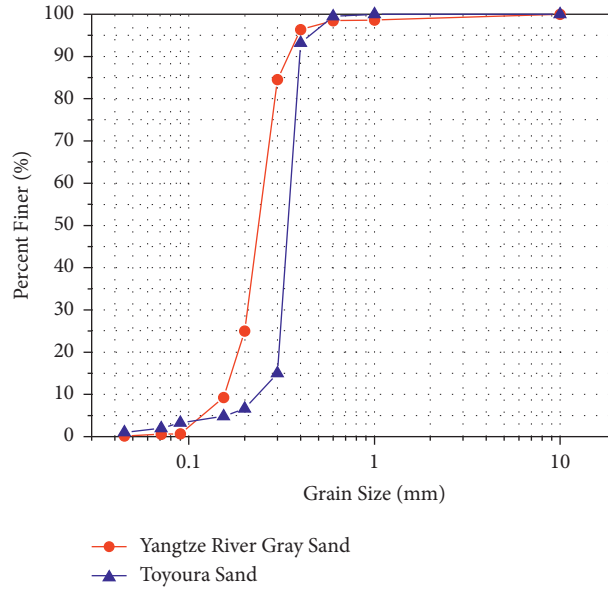
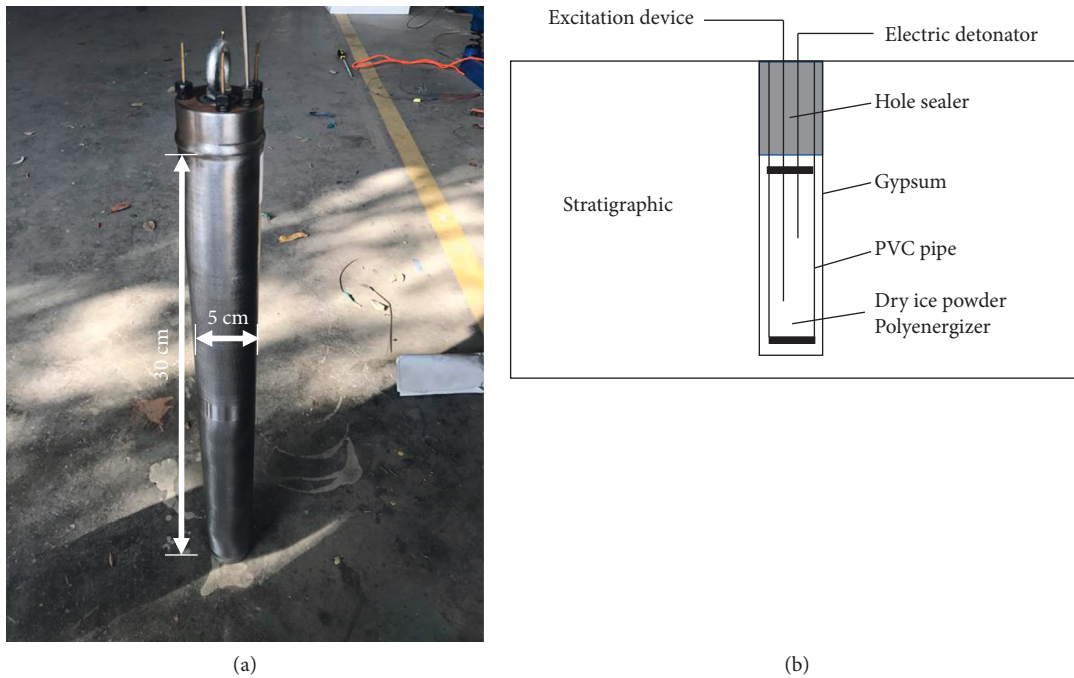Figure 2: Grading curve of the Yangtze River gray river sand.

(a)   (b)

Figure 3: CO_2 fracturing vessel and principle. (a) Physical image of the fracturing vessel. (b) Fracturing principle diagram.

vibration was calculated by using the field sand layer parameters obtained from the CPT, and the corresponding situation of the site was analyzed.

A CPT was performed at a location slightly distant from the two drainage rigid piles to reduce the disturbance to the sand around the piles. Fracturing container numbers 5–8 were filled with 680 g of dry ice, and the site ambient temperature was 2 degrees Celsius. The detonation sequence was simultaneous detonation of fissionable vessels numbered 5 and 7, and differential detonation of fissionable vessels numbered 8 and 6, where each fracture interval was approximately 2.5 s.

After completing the blast vibration test, a CPT was conducted on the sand layer again, and the relative density before and after the blast vibration was calculated by using the field sand layer parameters obtained from the CPT to analyze the corresponding situation of the site.

3. Results and Discussion

3.1. Comparison of the Site Phenomena after Blast Vibration. The changes in the site characteristics before and after the two tests were recorded using photographic equipment,
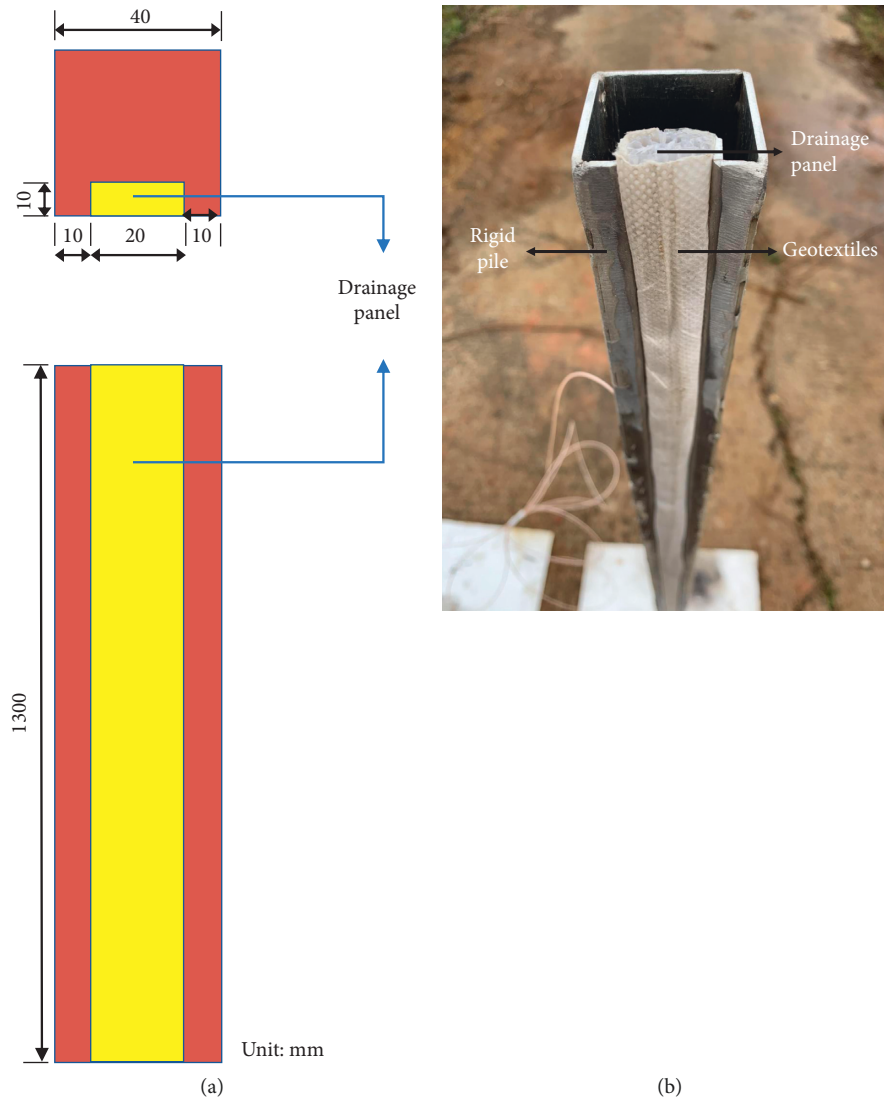
FIGURE 4: Schematic diagram of drainage rigid pile. (a) Dimensions of the drainage rigid pile. (b) Physical drawing of the drainage rigid pile.

and the comparison of the site before and after the simultaneous fracturing blast vibration test is shown in Figure 7.

As seen from Figure 7, after the blast vibration, water seeped out of the sand surface partly marked by the red squares, and slight settlement was produced on the surface part of the site after the vibration. On the drainage side of the drainage body of the rigid pile, i.e., the red circle part of the figure, it can be clearly seen that water gushed out of the sand surface through the drainage channel, while no water gush out on the side of the ordinary pile, so obviously the drainage channel played a role and facilitated the discharge of excess pore water.

A comparison of the site before and after the multiple fracturing blast vibration tests is shown in Figure 8.

It can be seen from Figure 8 that there was a significant difference between the multiple fracturing blast vibration tests and the simultaneous fracturing blast vibration test. Due to the increase in the dry ice content in the fracturing vessel, the fracturing power was significantly enhanced.

After the blast vibration, a large amount of water gushed out from the drainage channel on one side of the drainage rigid pile, while there was no obvious pore water gushing out around the ordinary pile, and the drainage performance of the drainage rigid pile was very excellent. As shown in the red squares in Figure 8, most areas of the site after blast vibration exhibited obvious settlement, and more pore water seepage out of the ground and in the settlement area formed an obvious puddle. A comparison between the drainage rigid pile and the ordinary pile during the blast is shown in Figure 9, which is a better visual comparison of the difference between the ordinary pile and the drainage rigid pile in handling the excess pore water inside the sand under the action of blast vibrations.

3.2. Relative Density Variation. Figure 10(a) shows the variation curve of the CPT cone tip resistance along the depth direction of the soil layer, and the measured results show that the cone tip resistance of the test sand layer is less
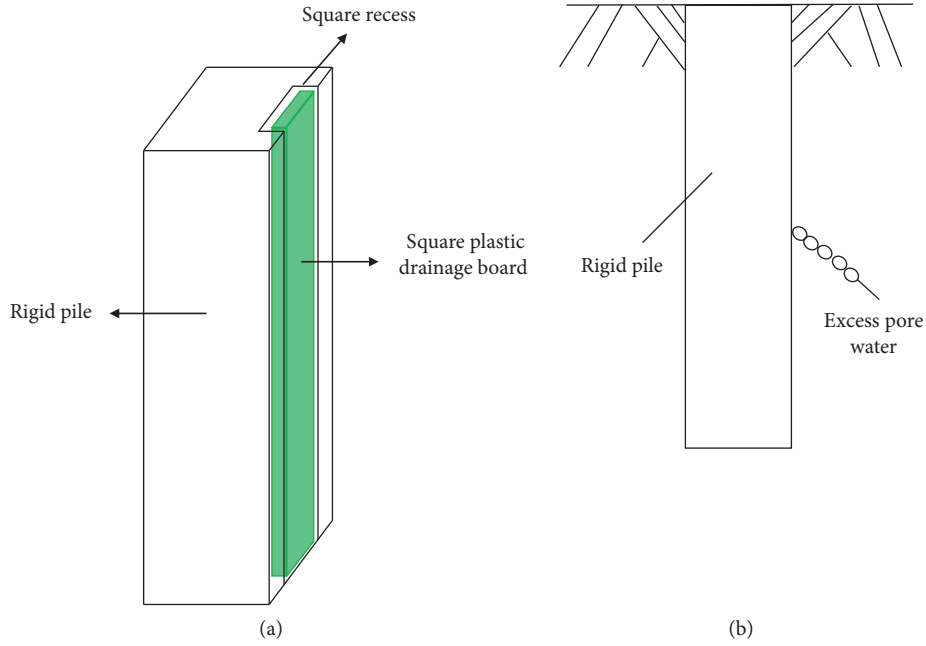
FIGURE 5: The operating principle of drainage rigid piles. (a) Composition of drainage rigid piles. (b) Principle of excess pore water dissipation.
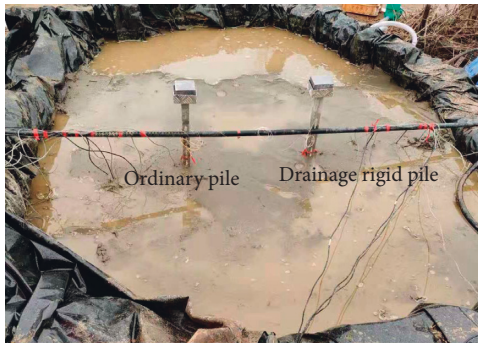

FIGURE 6: Final schematic of the site.

than 2 MPa. To obtain the relative density of the site, the in situ equation suggested by Jamiolkowski et al. [32] is used for the estimations in this study; this equation introduces a correction factor, considers the compressive nature of the soil, and presents an average relationship. The relative density along the depth of the soil layer can be expressed as an empirical function of the initial vertical effective stress and the CPT cone tip resistance, as shown in equation (1):

$$D_R = 100 \left[0.268 \ln \frac{q_c/p_a}{\sqrt{\sigma'_{v0}/p_a}} - 0.675 \right], \qquad (1)$$

where D_R is the initial relative density of the backfilled sand; σ'_{vo} is the initial vertical effective stress (kPa) at a depth in the soil; q_c is the CPT cone tip resistance (kPa); and p_a is the standard atmospheric pressure.

The initial relative density of the saturated soil layer is 35–55%, as calculated according to equation (1), where the deeper the sand layer is, the greater the relative density, as shown in Figure 10(b).
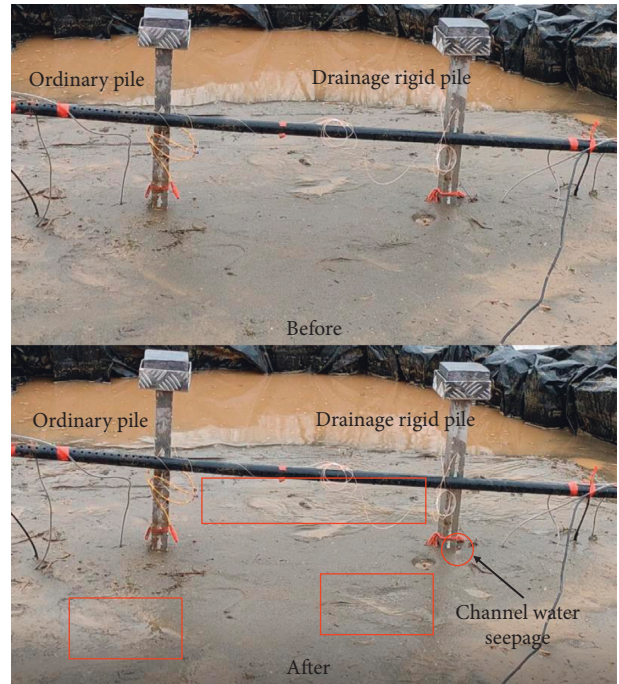

FIGURE 7: Comparison of before and after the simultaneous fracturing blast vibration test.

The relative density of the site after two blast vibrations calculated according to equation (1) is shown in Figure 11.

The relative density of the site after the simultaneous fracturing blast vibration test was 45%–60%, and the relationship curve between the relative density and the depth of the sand layer is shown in Figure 11(b). The relative density increased with the depth of the sand. This law is consistent
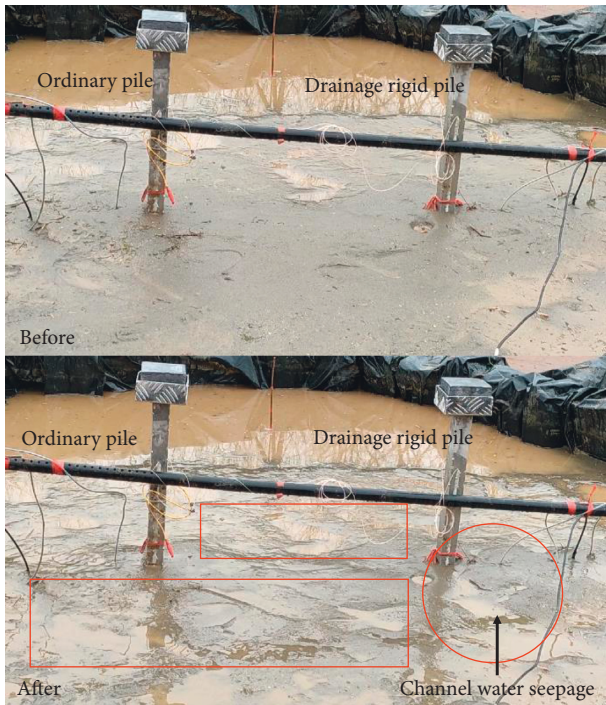
FIGURE 8: Comparison chart before and after multiple fracturing blast vibration tests.
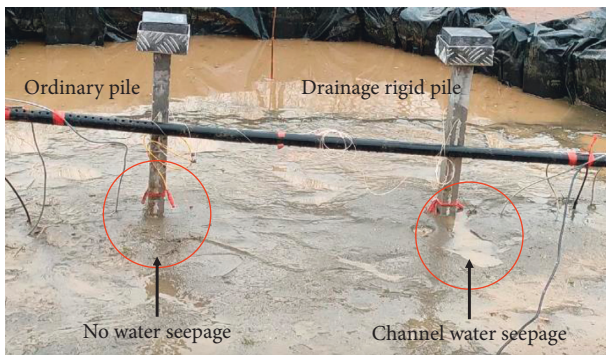

FIGURE 9: Schematic diagram of gushing water in the drainage channel.

with the law measured before the experiment. The relative density at the bottom of the sand layer is increased by 5%, while the relative density at the top of the sand layer increased by 10%.

The relative density of the site after the multiple fracturing blast vibration tests was 45%–65%, with the relationship curve between the relative density and the depth of the sand layer shown in Figure 11(d). Compared with the simultaneous fracturing blast vibration test, the increase in the relative density of the site was not significant because the site already had a certain degree of density after the simultaneous fracturing blast vibration test, and the relative density of the sand layer at each depth is increased by approximately 5%. The comparison graphs before and after the field test in Figure 8 show that a large area of uneven settlement occurred at the site, which needs to be further judged by the monitoring results of the field pore water

pressure. In general, the relative density of the site decreased with a decreasing depth of burial.

3.3. The Variation Pattern of Vertical Acceleration. As shown in Figure 1(b), according to the arrangement of the field equipment, the acceleration sensors on the side of the ordinary pile are numbered A1–A3 from top to bottom, and the pore water pressure sensors are numbered P1–P3; the acceleration sensors on the side of the drainage rigid pile are numbered A4–A6 from top to bottom, and the pore water pressure sensors are numbered P4–P6; the acceleration sensors at the bottom of the drainage rigid pile are numbered A7, and the acceleration sensors above the fracturing vessel are numbered A8. All acceleration sensors monitor the response of vertical acceleration.

The acceleration time curves of A7 and A8 at the bottom of the pit are shown in Figure 12. The A8 acceleration sensor was located directly above the fracturing vessel with a peak vertical acceleration of 6.643 g, and the A7 acceleration sensor was located at the bottom of the pile with a peak vertical acceleration of 2.674 g. The peak vertical acceleration of A7 was much smaller than the peak vertical acceleration of A8, which shows that the decay of vertical acceleration in the horizontal direction was more drastic.

Figure 13 shows the variation law of the peak vertical acceleration along the depth on the pile side during the blast vibration.

From the figure, the peak vertical acceleration variation law on both sides of the drainage rigid pile and the ordinary pile is consistent, the values are close, and there is no obvious difference. In the depth range of 1 m–0.4 m at the bottom of the pit, the acceleration peak decreased with depth, but there was a certain degree of acceleration amplification at measurement points A1 and A4 near the surface at the top. According to the research of previous scholars, the site and terrain had certain influences on the ground vibration parameters. For both horizontal and vertical acceleration, there was an amplification effect of acceleration at the ground surface [33], and measurement points A1 and A4 of this test were near the ground surface, so there was a certain amplification of the vertical acceleration.

The vertical acceleration time curves of A7 and A8 at the bottom of the pit under the effect of multiple fracturing blast vibrations are shown in Figure 14. The fracture sequence was the simultaneous fracture of vessels 5 and 7, followed by the fracture of vessel 8 for 2.5 s and finally vessel 6. The peak vertical acceleration of the A8 accelerometer directly above the fracturing vessel was 8.319 g and the peak vertical acceleration at the bottom of the drainage rigid pile was 3.262 g. The increase in the dry ice mass effectively improved the effect of the blast vibration, making the fracturing power more significant, resulting in a greater acceleration response of the site, and leading to an increase in the relative density of the site after the multiple fracturing blast vibration tests.

The variation pattern of the peak vertical acceleration along the depth of the pile side during the multiple fracture
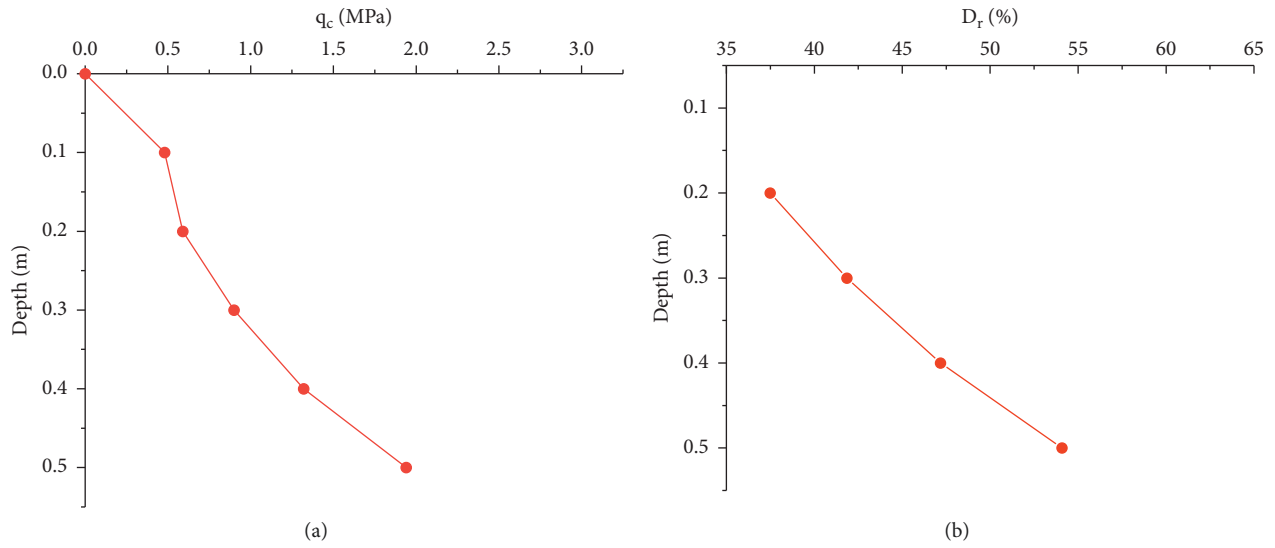
FIGURE 10: Initial site conditions. (a) The initial cone tip resistance variation curve of the site. (b) The initial relative site density.
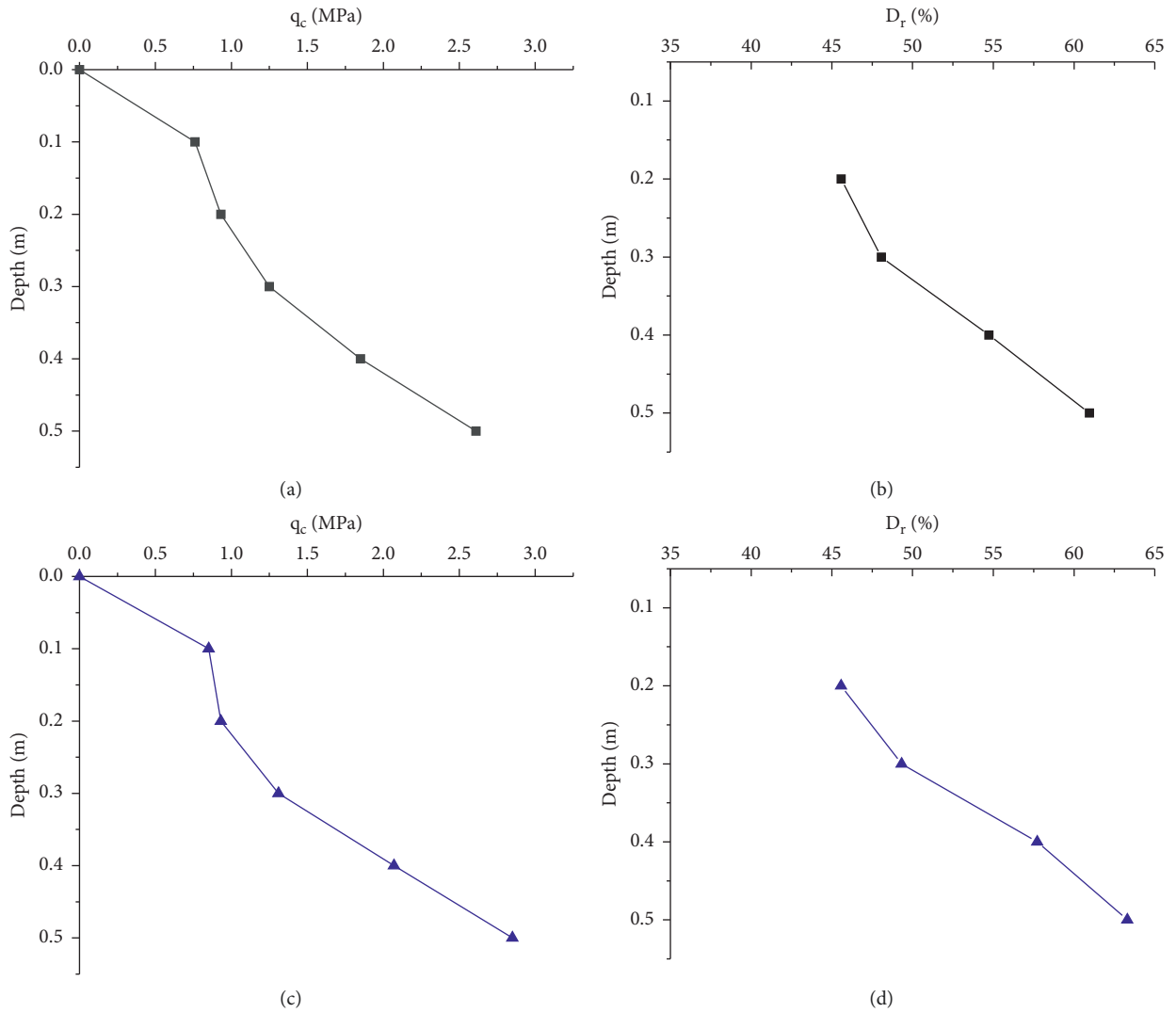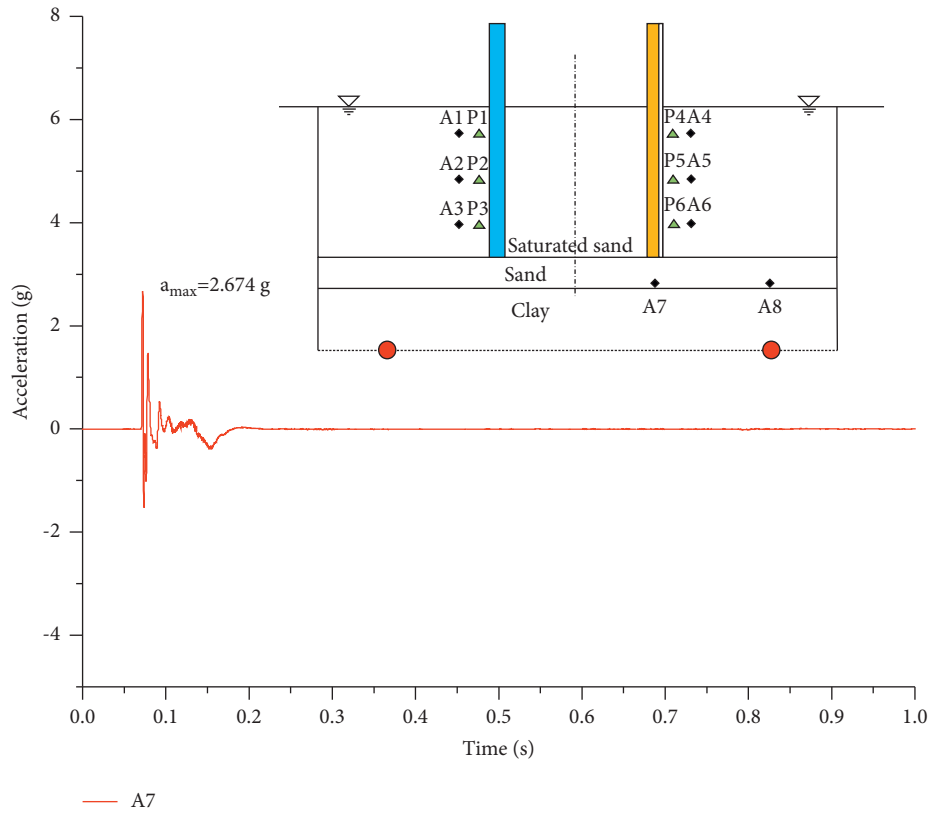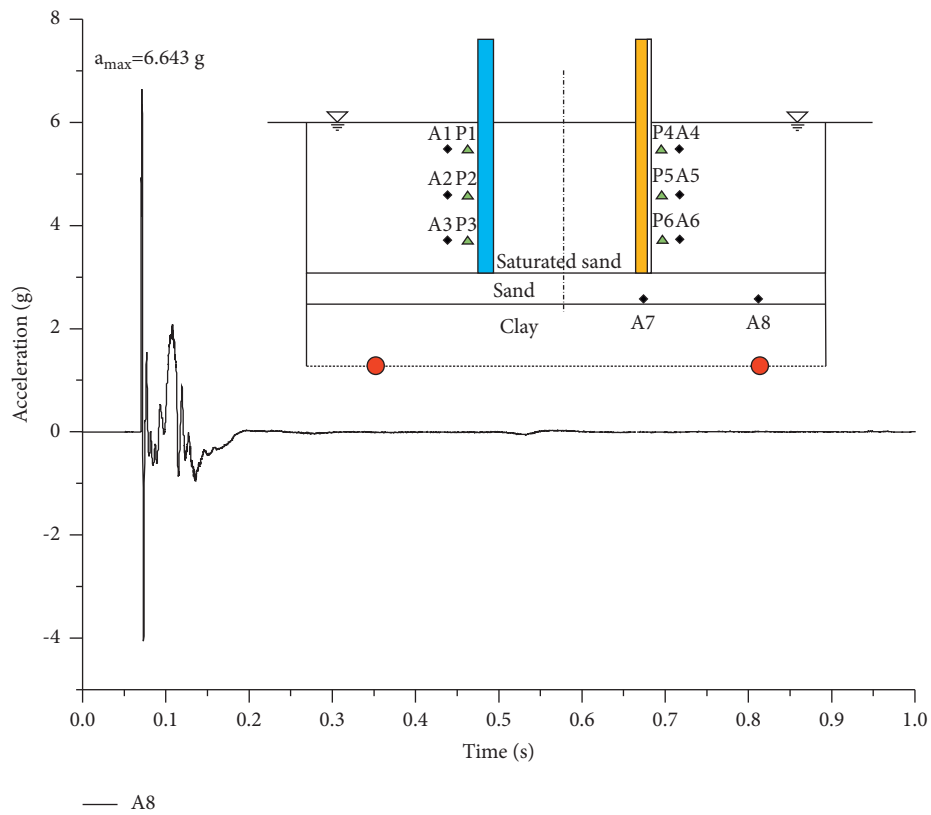

FIGURE 11: Condition of the site after the tests. (a) Cone tip resistance curve of the site after the simultaneous fracturing test, (b) relative density of the site after the simultaneous fracturing test, (c) cone tip resistance curve of the site after the multiple fracturing tests, and (d) relative density of the site after the multiple fracturing tests.

(a)

(b)

FIGURE 12: Vertical acceleration response of pit bottom after simultaneous fracturing blast vibration test. (a) Vertical acceleration time curve of the A7 sensor. (b) Vertical acceleration time curve of the A8 sensor.
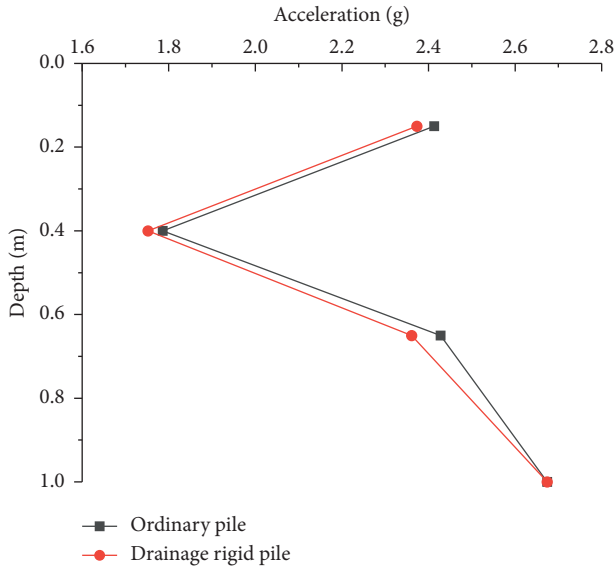
FIGURE 13: The variation pattern of the peak vertical acceleration along the depth on both sides of the ordinary pile and drainage rigid pile.

blast vibrations is shown in Figure 15. The peak vertical acceleration variation pattern was consistent with the simultaneous fracture test, except that the acceleration decay had more obvious changes.

3.4. Accumulation and Dissipation of the Pore Water Pressure.

When studying the problems associated with saturated sand foundations under the action of blast vibration, the main concern is whether or not the sand is liquefied. To discern whether or not the studied soil is liquefied, the ratio of the excess pore water pressure to the initial effective stress (PPR) is used to determine whether or not the soil is liquefied [34], and the expression of PPR is

$$PPR = \frac{\Delta u}{\sigma'_{v0}} \times 100\%, \tag{2}$$

where Δu is the excess pore water pressure (kPa) and σ_{vo}' is the initial effective stress (kPa). From equation (2), the PPR can be seen as a dimensionless scalar quantity.

The time course curves of the excess pore water pressure on both sides of the ordinary pile and the drainage rigid pile in the simultaneous fracturing blast vibration test are shown in Figure 16.

As shown in Figure 16, each burial depth of the site at the moment of blast vibration generated a certain degree of negative excess pore water pressure, and then the negative excess pore water pressure accumulated up to a positive excess pore water pressure. The reason was that at the moment of fracturing, the bottom of the site was impacted by the blast, resulting in the instantaneous expansion of the saturated sand in the site, which produced a greater suction on the pore water around both the drainage rigid piles and ordinary piles. However, the difference is that it took 1.5 s for the accumulation of

excess pore water pressure from a negative value to a positive value on the side of ordinary piles, while the excess pore water pressure on the side of drainage rigid piles rose to a positive value almost instantaneously, which shows that the drainage channel can accelerate the accumulation of excess pore water.

According to the time course curve, the peak excess pore water pressure of each pore water pressure sensor and the excess pore water pressure value after the dissipation of excess pore water were recorded, and then the PPR of the corresponding moment was calculated according to equation (2). The results are shown in Table 2.

The simultaneous fracturing blast vibration test caused a rise in the excess pore water pressure at the saturated sand foundation to not be particularly significant, as seen from the calculation results in Table 2. The two measurement points P3 and P6 with the deepest burial depth have the largest rise in excess pore water pressure. P3 was the measurement point on the side of the ordinary pile, the peak excess pore water pressure was 1.488 kPa, and the PPR was 0.25. P6 was the measurement point on the side of the drainage rigid pile, the peak excess pore water pressure was 1.741 kPa, and the PPR was 0.29. The P3 and P6 data were similar, which means that the site was not liquefied at a depth of 0.6 m. The peak PPR at the remaining burial depths did not meet the criteria for liquefaction, so it can be determined that the site did not meet the conditions for liquefaction in the simultaneous fracturing blast vibration test.

A comparison of Figure 16 and Table 2 shows that the time from peak dissipation to stabilization of excess pore water pressure on both sides of the ordinary pile and drainage rigid pile is not consistent. It took 12.71 s to dissipate the excess pore water pressure from peak to stable on the side of the ordinary pile, while it took 7.86 s on the side of the drainage rigid pile. The peak PPR was the smallest at a 0.4-m burial depth for both drainage rigid piles and ordinary piles, which indicated that the infiltration of pore water at the site was not uniform. It can be seen from the final dissipated PPR that the final distribution of excess pore water pressure was gradually reduced with a decreasing burial depth for both drainage rigid piles and ordinary piles.

In order to compare the ability of ordinary piles and drained rigid piles to finally dispose of excess pore water in saturated sand foundation, the magnitude of change of excess pore water pressure after dissipation to stability is used as an indicator. The dissipation value is obtained by subtracting the dissipated excess pore water pressure from the peak excess pore water pressure, and then dividing the dissipation value by the peak excess pore water pressure to obtain the dissipation magnitude, and the comparison graph is shown in Figure 17.

At a burial depth of 0.15 m, it can be seen that both the drainage rigid pile and the ordinary pile dissipated 99% of the excess pore water pressure, and that the excess pore water was almost dissipated because the burial depth of these two places was shallow, and the pore water can be discharged from the surface more easily. At a burial depth of 0.4 m, there was a clear difference between the two, with 39% dissipation
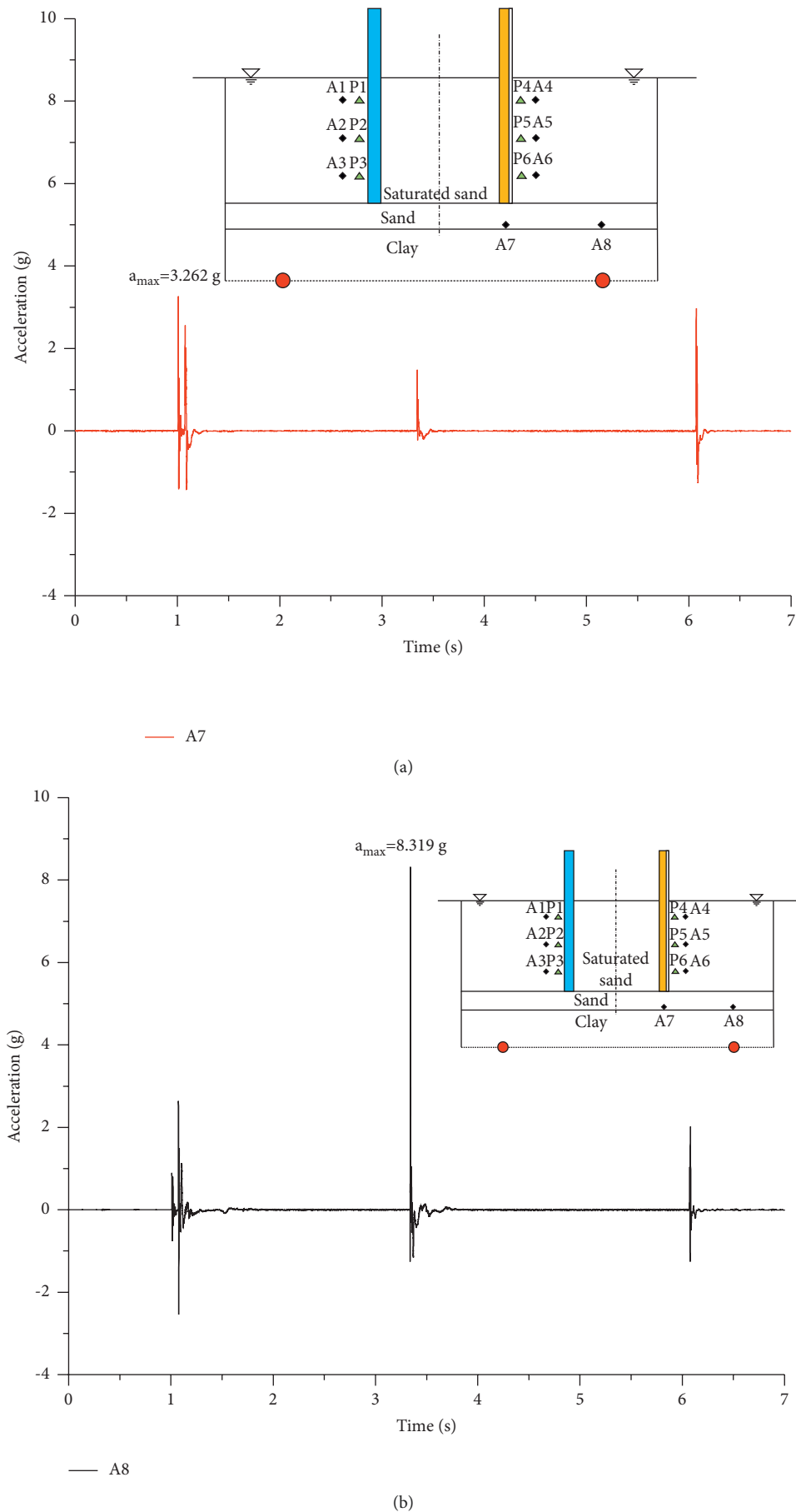
Figure 14: Vertical acceleration response of pit bottom after multiple fracturing blast vibration tests. (a) Vertical acceleration time curve of the A7 sensor. (b) Vertical acceleration time curve of the A8 sensor.
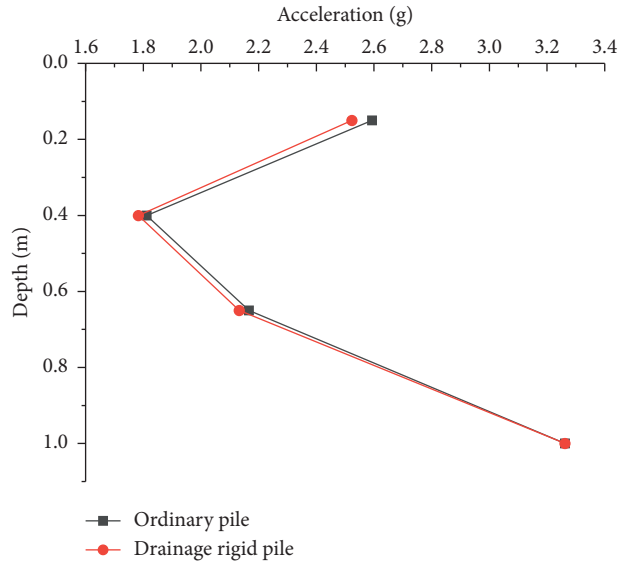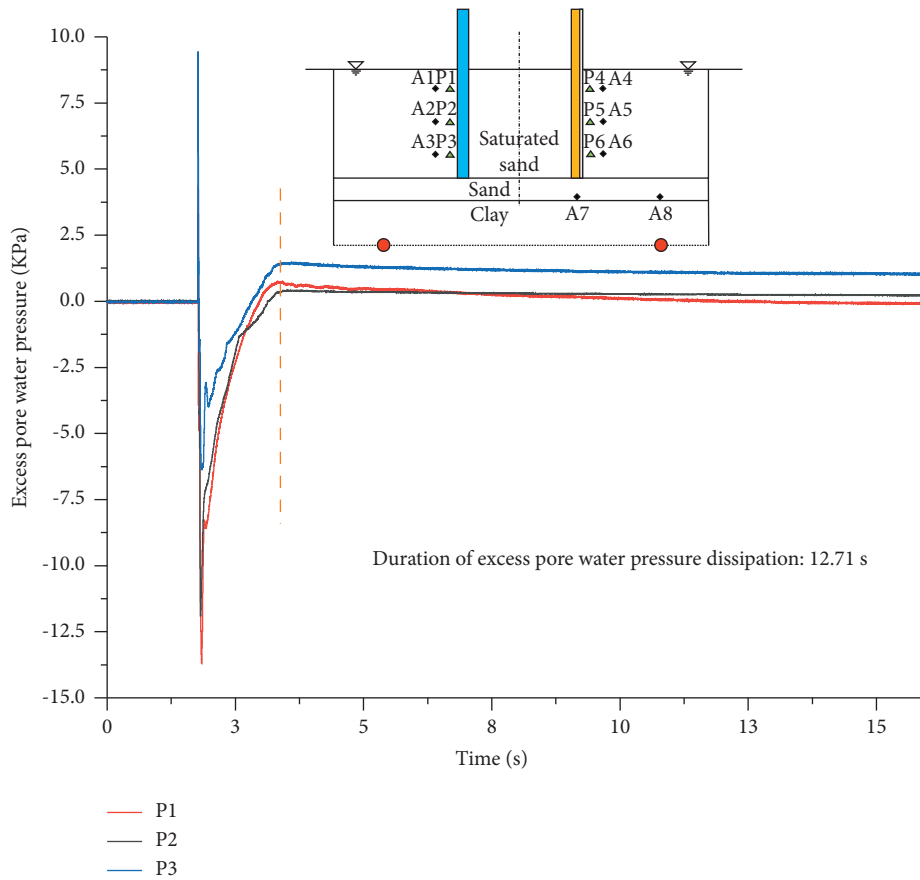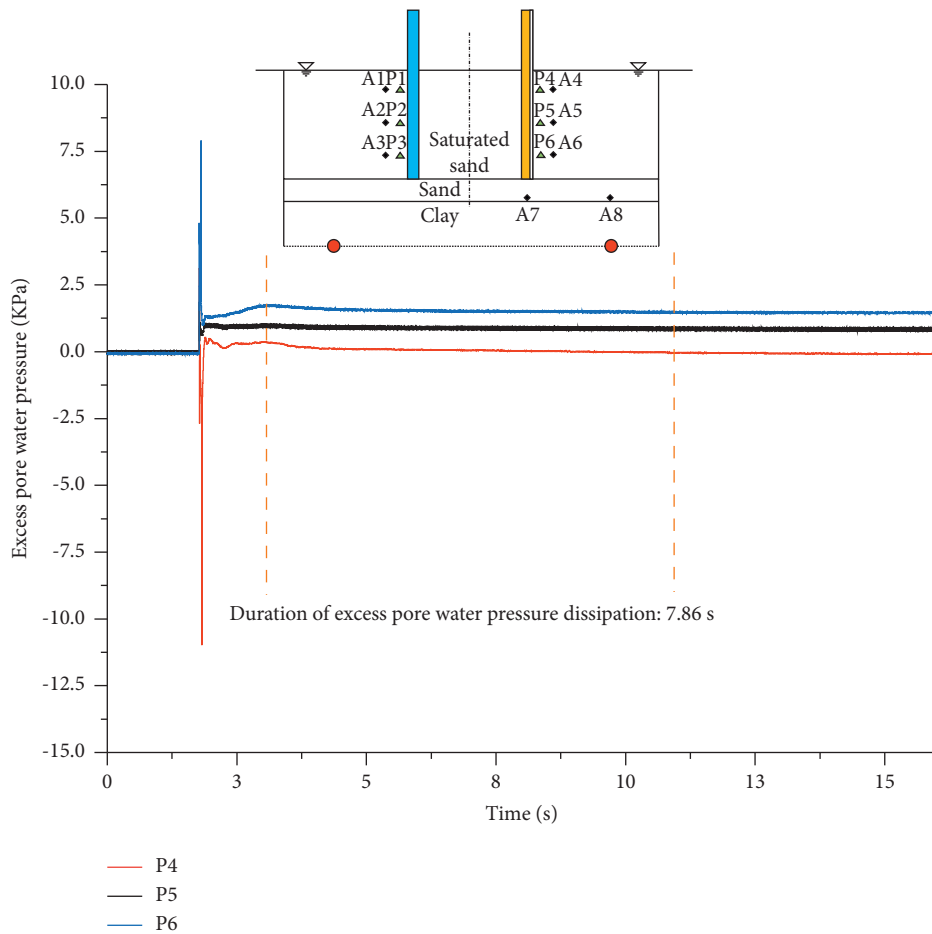
FIGURE 15: The variation pattern of peak vertical acceleration along the depth on both sides of the ordinary pile and the drainage rigid pile.

(a)

FIGURE 16: Continued.

(b)

FIGURE 16: Data from simultaneous fracturing blast vibration test. (a) Time course curve of excess pore water pressure in sand on one side of the ordinary pile. (b) Time course curve of excess pore water pressure in sand on one side of the drainage rigid pile.

TABLE 2: Excess pore water pressure and PPR of each measurement point.

Pore water pressure sensor	Peak excess pore water pressure/ kPa	Peak PPR	Excess pore water pressure after dissipation/kPa	PPR after dissipation
P1	0.661	0.48	0.005	0
P2	0.415	0.11	0.336	0.10
P3	1.488	0.25	1.173	0.20
P4	0.571	0.42	0.003	0
P5	1.013	0.28	0.610	0.16
P6	1.741	0.29	1.327	0.22

on the side of the drainage rigid pile and only 19% dissipation on the side of the ordinary pile. At a burial depth of 0.65 m, there was not much difference in the magnitude of dissipation between the two, but in general it was still slightly greater on the side of the drainage rigid pile than on the side of the ordinary pile. The drainage body on the side of the drainage rigid pile formed the drainage channel well, which favorably proves the working traits of the drainage rigid pile.

The time course curves of the excess pore water pressure on both sides of the ordinary pile and the drainage rigid pile in the multiple fracturing blast vibration tests are shown in Figure 18.

In a very short amount of time, the excess pore water pressure on both sides of the drainage rigid pile and the ordinary pile accumulated rapidly, from negative to positive, and at 2.5 s after the fracturing of containers 5 and 7, container 8 was fractured, at which time the excess pore water pressure did not accumulate to the peak on either side of the ordinary pile or drainage rigid pile. Under the action of the blast vibration load produced by the fracturing of container 8, the excess pore water pressure increased further and rapidly reached a maximum, and the excess pore water pressure was recorded as peak 1. Then the excess pore water pressure began to dissipate until the final container 6 cracked
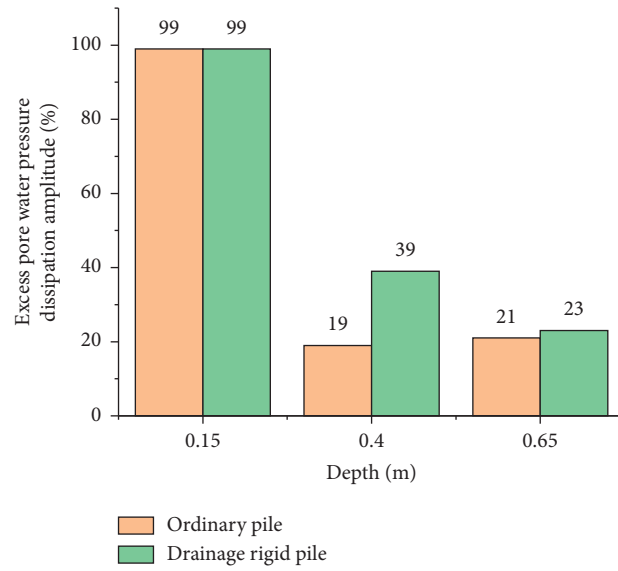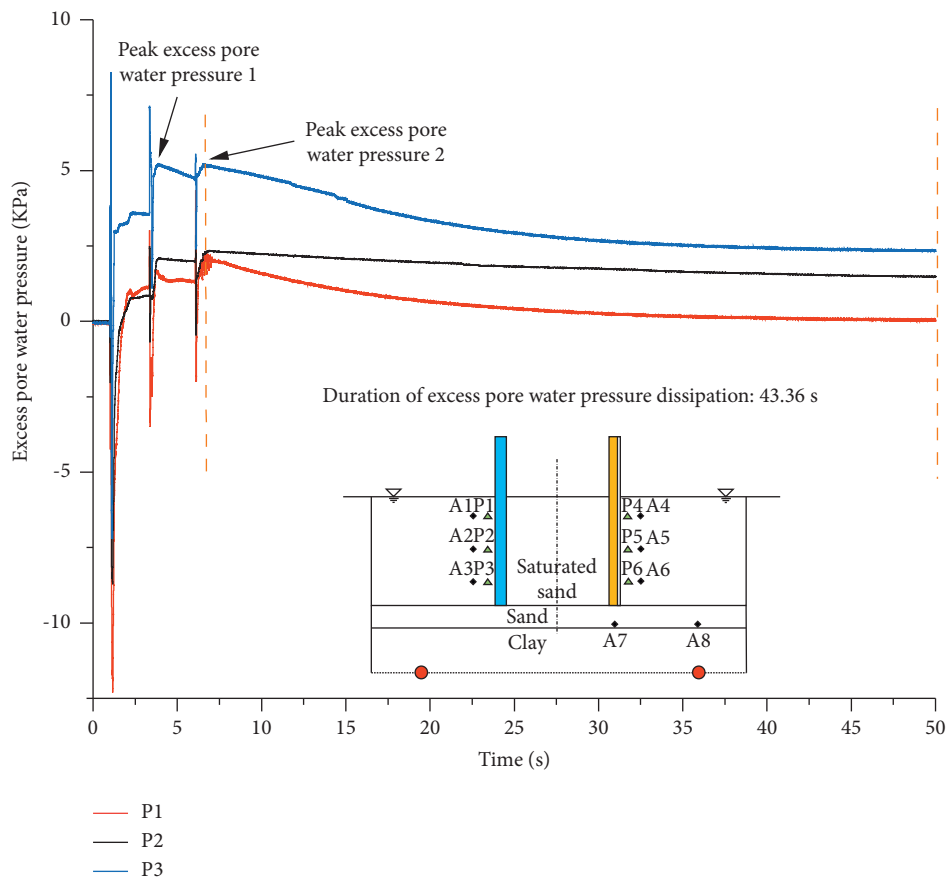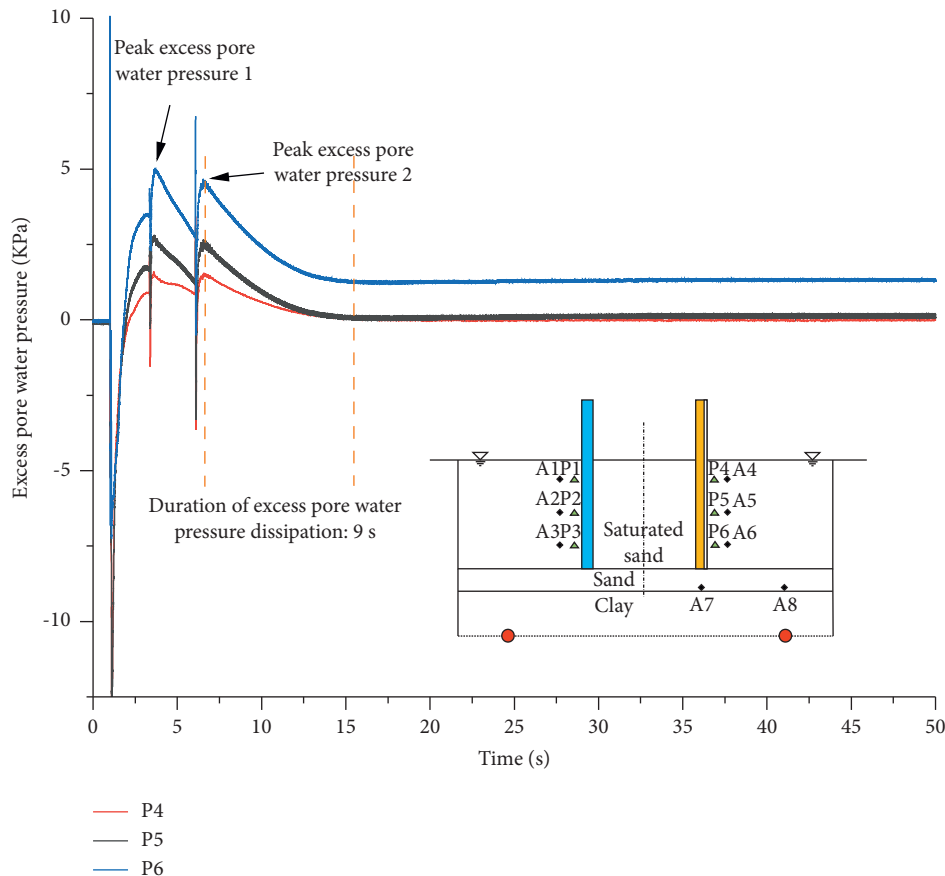
FIGURE 17: Dissipation magnitude of excess pore water pressure under the disposal of ordinary piles and drainage rigid piles in the simultaneous fracturing blast vibration test.

(a)

FIGURE 18: Continued.

FIGURE 18: (a) Time course curve of excess pore water pressure in sand on one side of the ordinary pile. (b) Time course curve of excess pore water pressure in sand on one side of the drainage rigid pile.

and the excess pore water pressure rose again. The maximum accumulated at this time was recorded as peak 2.

The excess pore water on one side of the ordinary pile leveled off before the accumulation of the vessel 8 fracture, and the slope of the time course curve was smaller, while the excess pore water pressure of the drainage rigid pile still maintained a fast rising trend before vessel 8 fractured, and the slope of the time course curve was larger, which indicated that the excess pore water could be rapidly discharged upward along the drainage channel due to the presence of the drainage body.

As shown in Figure 18, the time required to dissipate the excess pore water pressure from peak 2 to stability was 43.36 s for ordinary piles, while the time required for the drainage rigid piles was only 9 s. Compared with the simultaneous fracturing test, the larger the excess pore water pressure is, the greater the rigid pile of drainage rigid pile can play in the characteristic of rapid pore water pressure dissipation.

The excess pore water pressure at each moment was summarized, the corresponding PPR values were calculated, and the results are shown in Table 3.

According to the peak 2 PPR data of the ordinary pile measurement points, at a burial depth of 0.65 m the PPR reached 0.89; at this time, it can be considered that the saturated sand at a 0.65-m burial depth was close to liquefaction. At a burial depth of 0.4 m, the PPR was 0.64, which did not reach the level of liquefaction. At a 0.15-m burial depth, the PPR was 1.64, which was much larger than 1, the soil here was completely liquefied. Combined with the relative density plot of the site in Figure 11 and the peak acceleration plot in Figure 14, it is evident that during multiple blast vibrations the site's relative density did not change too much before and after the test, so the 0.65-m burial depth already had a high density. As the saturated sand at the bottom of the pit was most affected by the blast vibration, the site acceleration response was the largest and the site was prone to liquefaction, so the PPR was relatively close to liquefaction. The relative density of saturated sand in the range of 0.3–0.5 m varied greatly, indicating that the saturated sand was not completely densified and that the excess pore water could infiltrate upward more quickly, so the PPR at 0.4 m was smaller and liquefaction did not occur. The relative density at a 0.15-m depth was not significantly different before and after the two tests, but the acceleration near the surface at 0.15 m was somewhat amplified, and the excess pore water seeping upward from a 0.4-m depth made the excess pore water pressure increase rapidly at a 0.15-m depth, while the total soil stress at a 0.15-m depth was smaller and the relative compactness was lower here, so the

TABLE 3: Excess pore water pressure and PPR of each measurement point.

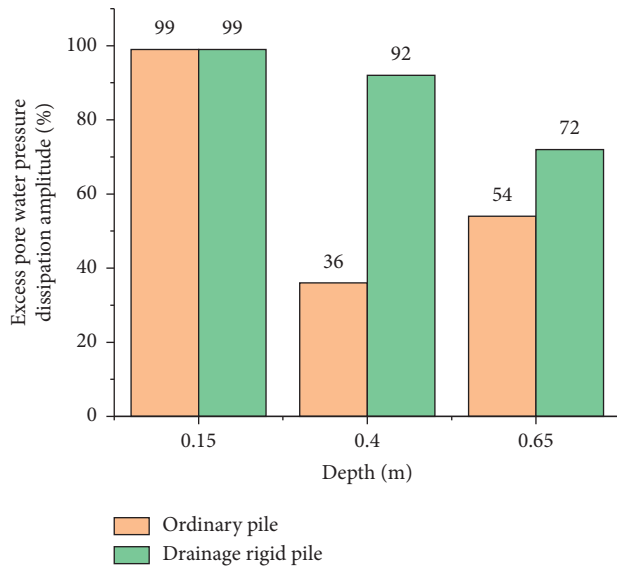| Pore water pressure sensor	Peak 1 excess pore water pressure/kPa	Peak 1 PPR	Peak 2 excess pore water pressure/kPa	Peak 2 PPR	Excess pore water pressure after dissipation/kPa	PPR after dissipation
P1	1.736	1.28	2.233	1.64	0.003	0
P2	2.100	0.58	2.346	0.64	1.493	0.40
P3	5.224	0.88	5.232	0.89	2.378	0.41
P4	1.593	1.17	1.550	1.14	0.002	0
P5	2.797	0.77	2.655	0.73	0.200	0.06
P6	5.015	0.85	4.675	0.80	1.289	0.22

FIGURE 19: Dissipation magnitude of excess pore water pressure under the disposal of ordinary piles and drainage rigid piles for multiple fracturing blast vibration tests.

PPR here reached 1.64, which was much larger than 1, leading to the saturated sand being completely liquefied.

According to the peak PPR data of the measured points of the drainage rigid pile, at a burial depth of 0.65 m, the PPR was 0.85, and the saturated sand here was close to liquefaction. At a burial depth of 0.4 m, the PPR was 0.77, which does not reach the liquefaction standard. At a burial depth of 0.15 m, the PPR was 1.17, which was greater than 1; obviously, the saturated sand here had been completely liquefied. Therefore, the liquefaction law of the soil on both sides of the drainage rigid pile and the ordinary pile is similar.

In order to compare the ability of ordinary piles and drainage rigid piles to finally dispose of excess pore water in saturated sand foundations, the magnitude of the change in excess pore water pressure from peak 2 dissipation to stabilization is used as an indicator, with the comparison graph shown in Figure 19.

After the dissipation was completed, the excess pore water on one side of the ordinary pile could also be smoothly dissipated. The final PPR was 0 because 0.15 m was close to the surface and the relative density of the site was approximately 45%. At a 0.4-m burial depth, the PPR of the ordinary pile side was 0.4, and the excess pore water pressure was dissipated by 36%, while the PPR of the drainage rigid

pile side was 0.06, and the excess pore water pressure was dissipated by 92%. At a depth of burial of 0.65 m, the PPR on the ordinary pile side was 0.41, with a 54% dissipation of the excess pore water pressure, while the PPR on the drainage rigid pile side was 0.22, with a 72% dissipation of the excess pore water pressure. Compared with the results of the simultaneous fracturing test, it can be seen that the higher the blast vibration load is, the higher the excess pore water pressure caused by the site, the more effective the drainage rigid pile is in dissipating the saturated excess pore water pressure, and the drainage rigid pile can dissipate a larger amount of excess pore water pressure in a shorter period of time.

4. Conclusions

In the fracturing blast vibration tests, the blast vibration load on the saturated sand foundation was generated by the CO_2 fracturing vessels. The responses of the saturated sand foundations under the disposal of ordinary piles and drainage rigid piles were compared. The main conclusions are as follows.

(1) The initial relative density of the saturated sand foundation was 35–55%, and the relative density of the site was 45–60% after the simultaneous fracturing blast vibration test. The relative density of the site was 45–65% after multiple fracturing blast vibrations. After the simultaneous fracturing test, the site was densified to a certain extent, so the increase in the site density after the multiple fracturing tests was not obvious. The vertical acceleration response patterns were similar for the two tests.

(2) In the simultaneous fracturing blast vibration test, the excess pore water pressure on the drainage rigid pile side rose to the peak instantaneously, while it took 1.5 s to reach the peak on the ordinary pile side. The dissipation time of the excess pore water was 12.71 s for the ordinary pile side, while it was 7.86 s for the drainage rigid pile side. The rate of excess pore water pressure rise on one side of the drainage rigid pile was also greater than that of the ordinary pile during multiple fracturing blast vibrations, and the dissipation time of the drainage rigid pile was shortened by approximately 34 s compared with that of the ordinary pile. This indicates that the drainage rigid pile can quickly accumulate excess pore water pressure and, likewise, quickly dissipate excess pore water pressure.

(3) In the simultaneous fracturing blast test, the final dissipation of the excess pore water pressure at depths of 0.4 m and 0.65 m on one side of the ordinary pile was 19% and 21%, while the dissipation under the action of drainage rigid piles was 39% and 23%. In the multiple fracturing blast tests, the final dissipation of excess pore water pressure at depths of 0.4 m and 0.65 m on one side of the ordinary pile was 36% and 54%, while the dissipation under the action of drainage rigid piles was 92% and 72%. The drainage channel plays a good role in terms of drainage, where the greater the excess pore water pressure is, the more obvious the effect of the drainage rigid piles.

(4) In multiple fracturing blast vibration tests, uneven liquefaction occurred at the saturated sand site, and the liquefaction patterns of the sand soil were the same on both sides of the ordinary pile and the drainage rigid pile; however, the PPR of the drainage rigid pile side in the near liquefaction or liquefaction region was smaller than that of the ordinary pile side, indicating that the drainage rigid pile could inhibit part of the accumulation of excess pore water pressure in the case of liquefaction, thus reducing the peak excess pore water pressure.

Data Availability

The data used to support the findings of this study are included within the article.

Conflicts of Interest

The authors declare that there are no conflicts of interest regarding the publication of this paper.

Acknowledgments

References

[1] M. Hamada, R. Isoyama, and K. Wakamatsu, "Liquefaction-induced ground displacement and its related damage to lifeline facilities," *Soils and Foundations*, vol. 36, pp. 81–97, 1996.

[2] L. Liu and R. Dobry, "Seismic response of shallow foundation on liquefiable sand," *Journal of Geotechnical and Geoenvironmental Engineering*, vol. 123, no. 6, pp. 557–567, 1997.

[3] P. Kirkwood and S. Dashti, "Considerations for the mitigation of earthquake-induced soil liquefaction in urban environments," *Journal of Geotechnical and Geoenvironmental Engineering*, vol. 144, no. 10, Article ID 04018069, 2018.

[4] R. Dobry and T. Abdoun, "Recent findings on liquefaction triggering in clean and silty sands during earthquakes," *Journal of Geotechnical and Geoenvironmental Engineering*, vol. 143, no. 10, Article ID 04017077, 2017.

[5] Y. Qiu and H. B. Mason, "Pore water pressure response of fully saturated soil beds during earthquake-tsunami multi-h," *Bulletin of the Seismological Society of America*, vol. 109, no. 5, pp. 1785–1796, 2019.

[6] A. Yamaguchi, T. Mori, M. Kazama, and N. Yoshida, "Liquefaction in tohoku district during the 2011 off the pacific coast of Tohoku earthquake," *Soils and Foundations*, vol. 52, no. 5, pp. 811–829, 2012.

[7] R. Sakamoto, S. Murakami, T. Nishi, and R. Hirata, "Liquefaction inside and outside bands and liquefaction layer characteristics related to the 2016 Kumamoto earthquake," *Springer Singapore*, vol. 62, 2020.

[8] S. Dashti, J. D. Bray, J. M. Pestana, M. Riemer, and D. Wilson, "Centrifuge testing to evaluate and mitigate liquefaction-induced building settlement mechanisms," *Journal of Geotechnical and Geoenvironmental Engineering*, vol. 136, no. 7, pp. 918–929, 2010.

[9] G. A. Narsilio, J. C. Santamarina, T. Hebeler, and R. Bachus, "Blast densification: multi-instrumented case history," *Journal of Geotechnical and Geoenvironmental Engineering*, vol. 135, no. 6, pp. 723–734, 2009.

[10] E. Sáez and C. Ledezma, "Liquefaction mitigation using secant piles wall under a large water tank," *Soil Dynamics and Earthquake Engineering*, vol. 79, pp. 415–428, 2015.

[11] F. Lopez-Caballero and A. Modaressi-Farahmand-Razavi, "Numerical simulation of mitigation of liquefaction seismic risk by preloading and its effects on the performance of structures," *Soil Dynamics and Earthquake Engineering*, vol. 49, pp. 27–38, 2013.

[12] L. Shao, D. Taylor, and M. Koelling, "Stone columns and earthquake drain liquefaction mitigation for federal center south in Seattle, Washington," in *Proceedings of the Washington. Geo-Congress 2013*, pp. 864–878, San Diego, California, U S A, March 2013.

[13] K. M. Rollins, L. J. Hales, and S. A. Ashford, "Camp, III, W.M. P-Y curves for large diameter shafts in liquefied sand from blast liquefaction tests," in *Proceedings of the Seismic Performance and Simulation of Pile Foundations in Liquefied and Laterally Spreading Ground*, pp. 11–23, California, United States, March2005.

[14] R. P. Orense, I. Towhata, and N. Chouw, "Soil liquefaction during recent large-scale earthquakes," *Soil Dynamics and Earthquake Engineering*, vol. 79, p. 279, 2015.

[15] s. Yasuda, i. Towhata, i. Ishii, s. Sato, and t. Uchimura, "Liquefaction-Induced damage to structures during the 2011 great east Japan earthquake," *Journal of JSCE*, vol. 1, no. 1, pp. 181–193, 2013.

[16] K. Otsushi, T. Kato, T. Hara et al., "Study on a liquefaction countermeasure for flume structure by sheet-pile with drain," in *Proceedings of the Geotechnical Society of Singapore—International Symposium on Ground Improvement Technologies and Case Histories*, pp. 437–443, Singapore, January 2010.

[17] K. Adalier, A. Pamuk, and T. F. Zimmie, "Earthquake retrofit of highway/railway embankments by sheet-pile walls," *Geotechnical & Geological Engineering*, vol. 22, no. 1, pp. 73–88, 2004.

[18] K. Otsushi, T. Kato, T. Hara et al., "Analytical study on mitigation of liquefaction-related damage to flume channel using sheet-pile with drain," in *Proceedings of the GeoFlorida 2010*, pp. 3062–3071, Orlando, Florida, United States, February 2010.

[19] A. Eslami, "Investigation of explosive compaction (EC) for liquefaction mitigation using CPT records," *Bulletin of Earthquake Engineering*, vol. 13, no. 11, pp. 3239–3257, 2015.

[20] R. Daryaei and A. Eslami, "Settlement evaluation of explosive compaction in saturated sands," *Soil Dynamics and Earthquake Engineering*, vol. 97, pp. 241–250, 2017.

[21] M. Esmaeili and B. Tavakoli, "Finite element method simulation of explosive compaction in saturated loose sandy soils," *Soil Dynamics and Earthquake Engineering*, vol. 116, pp. 446–459, 2019.

[22] B. Tavakoli and M. Esmaeili, "Numerical evaluation of square arrangement of charges in explosive compaction," *Soil Dynamics and Earthquake Engineering*, vol. 130, Article ID 106001, 2020.

[23] M. Goodarzi, S. Mohammadi, and A. Jafari, "Numerical analysis of rock fracturing by gas pressure using the extended finite element method," *Petroleum Science*, vol. 12, no. 2, pp. 304–315, 2015.

[24] S. Mohammadi and A. Bebamzadeh, "A coupled gas-solid interaction model for FE/DE simulation of explosion," *Finite Elements in Analysis and Design*, vol. 41, no. 13, pp. 1289–1308, 2005.

[25] S. McHugh, "Crack extension caused by internal gas pressure compared with extension caused by tensile stress," *International Journal of Fracture*, vol. 21, no. 3, pp. 163–176, 1983.

[26] G. W. Ma and X. M. An, "Numerical simulation of blasting-induced rock fractures," *International Journal of Rock Mechanics and Mining Sciences*, vol. 45, no. 6, pp. 966–975, 2008.

[27] A. Verhaven, T. Doneux, and D. Bizzotto, "Application of FRET microscopy to the study of the local environment and dynamics of DNA SAMs on Au electrodes," *Langmuir*, vol. 34, no. 49, pp. 14802–14810, 2018.

[28] M. G. Jaimes, R. D. Castillo, and S. A. Mendoza, "High energy gas fracturing: a technique of hydraulic prefracturing to reduce the pressure losses by friction in the near wellbore—a Colombian field application," *The Day*, vol. 2, pp. 919–930, 2012.

[29] Z. Yan, S. Hu, Y. Bian, S. Pang, and Q. Wang, "Experimental study on the mass ratio of dry ice powder pneumatic fracturing concrete," *Eng. Blasting*, vol. 25, pp. 14–18, 2019.

[30] K. Rollins, J. K. Anderson, R. R. Goughnour, and A. K. Mccain, "Liquefaction hazard mitigation using vertical composite drains," in *Proceedings of the 13th World Conference on Earthquake Engineering*, p. 2880, Canada, August 2004.

[31] H.-l. Liu, Y.-m. Chen, and N. Zhao, "Development technology of rigidity-drain pile and numerical analysis of its anti-liquefaction characteristics," *Journal of Central South University of Technology*, vol. 15, no. S2, pp. 101–107, 2008.

[32] M. Jamiolkowski, D. C. F. Lo Presti, and M. Manassero, "Evaluation of relative density and shear strength of sands from CPT and DMT," *In Proceedings of the Soil Behavior and Soft Ground Construction*, vol. 119, pp. 201–238, 2003.

[33] A. Liu, T. Liu, Y. Cui, and H. Zheng, "Discussion on the site effect coefficient and topographic effect coefficient of ground motion peak acceleration and its relationship," *IOP Conference Series: Earth and Environmental Science*, vol. 218, Article ID 012095, 2019.

[34] P. Knodel, W. Charlie, P. Jacobs, and D. Doehring, "Blast-induced liquefaction of an alluvial sand deposit," *Geotechnical Testing Journal*, vol. 15, no. 1, pp. 14–23, 1992.